

# Influence of Fe and Co Content on Crystallization and Magnetic Property of FeZrB Alloys

ZHONG HUA<sup>a,\*</sup>, TAOTAO FENG<sup>a</sup>, YUECHENG WU<sup>a</sup>,  
WANQIU YU<sup>b</sup> AND PINGLI ZHANG<sup>b</sup>

<sup>a</sup>General Education Center, Quanzhou University of Information Engineering, 362000 Quanzhou, China

<sup>b</sup>College of Physics, Jilin Normal University, 136000 Siping, China

Received: 09.11.2022 & Accepted: 20.12.2022

Doi: [10.12693/APhysPolA.143.270](https://doi.org/10.12693/APhysPolA.143.270)

\*e-mail: [hz196110@126.com](mailto:hz196110@126.com)

Substituting Fe with Co in Fe-based alloys to adjust the composition and optimize properties is a hot topic. Amorphous  $\text{Fe}_{84-x}\text{Co}_x\text{Zr}_7\text{B}_9$  ( $x = 0, 7, 14, 21, 28, 35, 42$ ) ribbons were prepared and annealed at their first exothermic peak temperature. The crystallization and magnetic properties of the alloys can be divided into two regions. The first region corresponds to the  $\text{Fe}_{84-x}\text{Co}_x\text{Zr}_7\text{B}_9$  ( $x = 0, 7, 14, 21$ ) alloys, and the second region corresponds to the  $\text{Fe}_{84-x}\text{Co}_x\text{Zr}_7\text{B}_9$  ( $x = 28, 35, 42$ ) alloys. There are four exothermic peaks for  $\text{Fe}_{84-x}\text{Co}_x\text{Zr}_7\text{B}_9$  ( $x = 0, 7, 14, 21$ ) alloys, and there are three crystallization exothermic peaks for  $\text{Fe}_{84-x}\text{Co}_x\text{Zr}_7\text{B}_9$  ( $x = 28, 35, 42$ ) alloys during crystallization. Only a single phase precipitates from the amorphous matrix for all alloys after annealing. With the increase in Co content, the lattice constant first increases up to 21 at.% Co and then decreases. The crystallization volume fraction ( $V_{\text{cry}}$ ) and the grain size ( $D$ ) continue to decrease. When the Co content is 21 at.%, there is little change in Co concentration between the nanocrystal and the remaining amorphous matrix. When the Co content is 42 at.%, the Fe content in the remaining amorphous matrix is significantly less than that in the nanocrystal, and the Co content in the remaining amorphous matrix is slightly higher than that in the nanocrystal. The content of Fe in the nanocrystal is higher than that of Co in the nanocrystal. The specific saturation magnetization  $M_s$  of as-quenched alloys and annealed alloys increases sharply up to 28 at.% Co and then decreases with a further increase in the Co content. The  $M_s$  values of annealed alloys are greater than those of as-quenched alloys. The coercivity  $H_c$  values of annealed alloys are lower than those of as-quenched alloys. For  $\text{Fe}_{84-x}\text{Co}_x\text{Zr}_7\text{B}_9$  ( $x = 0, 7, 14, 21$ ) alloys, the higher the Co content, the higher the difference between the  $H_c$  values of as-quenched and annealed alloys. For  $\text{Fe}_{84-x}\text{Co}_x\text{Zr}_7\text{B}_9$  ( $x = 28, 35, 42$ ) alloys, the difference between the  $H_c$  values of as-quenched and annealed alloys is small.

topics: amorphous alloy, Co content, crystallization, microstructure

## 1. Introduction

Fe(Co)-based alloys have higher Curie temperatures and higher magnetization compared to other Fe-based alloys without Co, resulting in potential applications at higher operating temperatures, which have been widely reported [1–7]. Furthermore, scholars have paid attention to the effect on structure [4–9], thermal property [9, 10], magnetic property [10–17], and application [18, 19] of using Co to replace Fe in the alloys.

For  $\text{Fe}_{83.2-x}\text{Co}_x\text{B}_{10}\text{C}_6\text{Cu}_{0.8}$  (where  $x = 0–10$ ) alloys [10], the doping of Co can effectively regulate the Curie temperature and magnetic properties of alloys. For  $(\text{Fe}_{1-x}\text{Co}_x)_{86}\text{Hf}_7\text{B}_6\text{Cu}_1$  ( $x = 0–1$ ) alloys [14], the lattice parameter of nanoscale precipitation decreased with increasing Co content because of the high solubility of Co in the  $\alpha(\alpha')$ -Fe(Co) solid

solution. For  $\text{Fe}_{80}\text{Co}_x\text{B}_{14-x}\text{Si}_2\text{P}_3\text{Cu}_1$  ( $x = 0, 2, 4, 6$ ) alloy ribbons [16], the addition of Co decreased the thermal stability of the alloy to crystallization and expanded the heat treatment temperature region of this family of alloy. For  $\text{Fe}_{61+x}\text{Co}_{10-x}\text{Y}_8\text{W}_1\text{B}_{20}$  ( $x = 0, 1, 2$ ) bulk amorphous alloys [17], a change in the Co content resulted in measurable effects on the Curie temperature and the value of the coercive field but had little effect on the saturation of the magnetization. For  $(\text{Fe}_{1-x}\text{Co}_x)_{84}\text{Zr}_{3.5}\text{Nb}_{3.5}\text{B}_8\text{Cu}_1$  ( $x = 0.0–0.8$ ) alloys [20], the crystallization temperature  $T_x$  of the amorphous alloy decreased with increasing Co content, whereas the Curie temperature  $T_C$  of the amorphous alloy was enhanced by the increase in the Co content.

The magnetic properties of Fe-based amorphous-nanocrystalline alloys are closely related to their microstructure. It is very important to explore the

effect of Co content on the crystallization and magnetic properties of Fe-based amorphous alloys. Especially after adding Co into the Fe-based alloy, the distribution ratios of Fe and Co in the crystalline phase and in the remaining amorphous phase are different, which further affects the crystallization of the alloys and results in differences in the structure and properties of FeCo-based nanocrystalline alloys with different Fe and Co ratios. Substituting Fe with Co in Fe-based alloys to adjust the composition and optimize properties is still a hot topic.

In this paper,  $\text{Fe}_{84-x}\text{Co}_x\text{Zr}_7\text{B}_9$  ( $x = 0, 7, 14, 21, 28, 35, 42$ ) amorphous alloys were prepared and annealed at their respective first exothermic peak temperature. The thermal behavior, microstructure, and magnetic properties of alloys have been investigated. The effect of Co content on the crystallization and magnetic properties of FeZrB alloys was studied in detail. Especially after adding different Co content into the alloy, the distribution ratios of Fe and Co in the crystalline phase and in the remaining amorphous phase were investigated. The crystallization and magnetic properties of the FeCoZrB alloys can be divided into two regions. By exploring the law of the microstructure change of the primary crystallization phase of the FeZrB amorphous alloy caused by the change in Fe and Co content, we can purposefully guide the research and development of this kind of alloy materials.

## 2. Experimental details

Alloy ingots with nominal compositions  $\text{Fe}_{84-x}\text{Co}_x\text{Zr}_7\text{B}_9$  ( $x = 0, 7, 14, 21, 28, 35, 42$ ) were prepared by induction melting the mixtures of high-purity Fe (99.98 wt%), Co (99.99 wt%), Zr (99.92 wt%), and B (99.999 wt%). High-purity Ti as a getter was melted to remove residual oxygen that might be present in the chamber. The ingots were remelted 4 times with magnetic stirring under the protection of a high-purity argon atmosphere to ensure homogeneity. Amorphous ribbons about 10 mm wide and 30  $\mu\text{m}$  thick produced from the ingots were prepared by a single roller melt spinning with a copper wheel rotating at a surface velocity of 38 m/s under the protection of a high-purity argon atmosphere. The amorphous ribbons were annealed at the first exothermic peak temperature from differential scanning calorimetry (DSC) traces in the furnace at vacuum.

DSC traces of amorphous alloys were investigated by simultaneous thermal analyzer (STA) (STA 449 F5). Structural characterizations of samples were examined by X-ray diffraction (XRD) (D/max 2500 PC, Cu  $K_\alpha$ ,  $\lambda = 1.5406 \text{ \AA}$ ) and transmission electron microscopy (TEM) (FEI Talos F200). TEM and energy dispersive spectroscopy (EDS) were taken on FEI Talos F200X. A precision ion polishing system (PIPS) (Gatan 695) was used to prepare TEM samples. The lattice constant and grain size

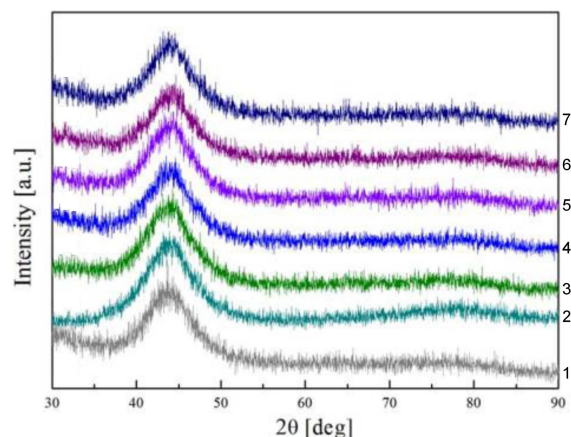


Fig. 1. XRD patterns of  $\text{Fe}_{84-x}\text{Co}_x\text{Zr}_7\text{B}_9$  ( $x = 0, 7, 14, 21, 28, 35, 42$ ) as-quenched alloys; (1)  $\text{Fe}_{84}\text{Zr}_7\text{B}_9$ , (2)  $\text{Fe}_{77}\text{Co}_7\text{Zr}_7\text{B}_9$ , (3)  $\text{Fe}_{70}\text{Co}_{14}\text{Zr}_7\text{B}_9$ , (4)  $\text{Fe}_{63}\text{Co}_{21}\text{Zr}_7\text{B}_9$ , (5)  $\text{Fe}_{56}\text{Co}_{28}\text{Zr}_7\text{B}_9$ , (6)  $\text{Fe}_{49}\text{Co}_{35}\text{Zr}_7\text{B}_9$ , and (7)  $\text{Fe}_{42}\text{Co}_{42}\text{Zr}_7\text{B}_9$ .

are calculated by MDI Jade 5.0. The specific saturation magnetization ( $M_s$ ) was obtained by a vibrating sample magnetometer (VSM) (Lake Shore M7407). Coercivity ( $H_c$ ) was measured by a direct current (DC) B-H loop tracer (RIKEN BHS-40).

## 3. Results and discussion

Figure 1 shows the XRD patterns of the  $\text{Fe}_{84-x}\text{Co}_x\text{Zr}_7\text{B}_9$  ( $x = 0, 7, 14, 21, 28, 35, 42$ ) as-quenched alloys. No crystalline diffraction peaks are observed, indicating that the as-quenched alloys are all fully amorphous.

The DSC traces of  $\text{Fe}_{84-x}\text{Co}_x\text{Zr}_7\text{B}_9$  ( $x = 0, 7, 14, 21, 28, 35, 42$ ) amorphous alloys are shown in Fig. 2. For  $\text{Fe}_{84-x}\text{Co}_x\text{Zr}_7\text{B}_9$  ( $x = 0, 7, 14, 21$ ) alloys, there are four exothermic peaks during the crystallization. For  $\text{Fe}_{84-x}\text{Co}_x\text{Zr}_7\text{B}_9$  ( $x = 28, 35, 42$ ) alloys, there are three crystallization exothermic peaks during the crystallization. With the increase in Co content, the intensity of the first ( $T_{p1}$ ) and the third ( $T_{p3}$ ) crystallization exothermic peaks is slightly enhanced, and the values of a peak temperature shift to the low-temperature direction. The second ( $T_{p2}$ ) exothermic crystallization peak temperature decreases up to 21 at.% Co and then increases with the increase in Co content. When the atomic percent of Co is between 0 to 21, the fourth ( $T_{p4}$ ) crystallization peak temperature shifts to the high-temperature direction. Three or four exothermic peaks were observed in the DSC curves of FeCoZrB series alloys, indicating that the crystallization processes of the series alloys were multistage crystallization.

XRD patterns of  $\text{Fe}_{84-x}\text{Co}_x\text{Zr}_7\text{B}_9$  ( $x = 0, 7, 14, 21, 28, 35, 42$ ) amorphous alloys annealed at the first exothermic peak temperature are shown

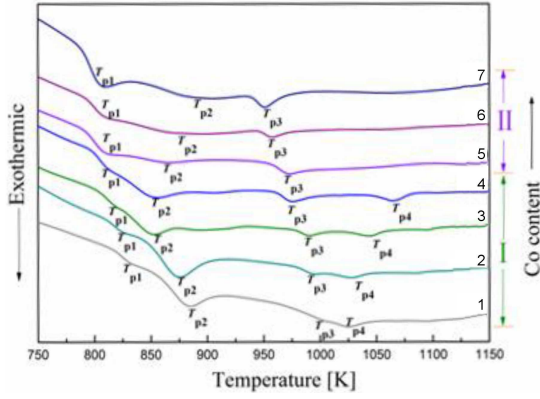


Fig. 2. DSC traces of  $\text{Fe}_{84-x}\text{Co}_x\text{Zr}_7\text{B}_9$  ( $x = 0, 7, 14, 21, 28, 35, 42$ ) amorphous alloys; (1)  $\text{Fe}_{84}\text{Zr}_7\text{B}_9$ , (2)  $\text{Fe}_{77}\text{Co}_7\text{Zr}_7\text{B}_9$ , (3)  $\text{Fe}_{70}\text{Co}_{14}\text{Zr}_7\text{B}_9$ , (4)  $\text{Fe}_{63}\text{Co}_{21}\text{Zr}_7\text{B}_9$ , (5)  $\text{Fe}_{56}\text{Co}_{28}\text{Zr}_7\text{B}_9$ , (6)  $\text{Fe}_{49}\text{Co}_{35}\text{Zr}_7\text{B}_9$ , and (7)  $\text{Fe}_{42}\text{Co}_{42}\text{Zr}_7\text{B}_9$ .

in Fig. 3. It can be seen that only  $\alpha$ -Fe phase precipitates from the amorphous matrix for all alloys. With the increase in Co content, the diffraction peak (110) first shifts to the low angle up to 21 at.% Co and then slightly to the high angle. The crystallization volume fraction ( $V_{\text{cry}}$ ) decreases. The FWHM (full width at half maxima) of the diffraction peak increases gradually, which indicates that the average grain size decreases with the increase in Co content.

Grain size ( $D$ ) and lattice constant of  $\text{Fe}_{84-x}\text{Co}_x\text{Zr}_7\text{B}_9$  ( $x = 0, 7, 14, 21, 28, 35, 42$ ) amorphous alloys annealed at their first exothermic peak temperature are given in Fig. 4. With the increase in Co content, the grain size of  $\alpha$ -Fe continued to decrease. According to the works by A. Takeuchi et al. [21], the heat of mixing of Co-Fe is  $-1$  kJ/mol. The heat of mixing of Co-B ( $-24$  kJ/mol) is close to that of Fe-B ( $-26$  kJ/mol), but the heat of mixing of Co-Zr ( $-41$  kJ/mol) is larger than that of Fe-Zr ( $-25$  kJ/mol). Therefore, substituting Fe with Co increases the density and viscosity of liquid atoms, which leads to atom rearrangement. After crystallization, the distribution ratio of element atoms in the crystallization phase is different, which leads to a difference of the lattice constant. The crystallization phase  $\alpha$ -Fe has a body-centered cubic structure (bcc). The lattice constants of pure  $\alpha$ -Fe and pure  $\alpha$ -FeCo are  $2.8664$  and  $2.8550$  Å, respectively. For Co-free alloys, the lattice constant of the  $\alpha$ -Fe phase is much lower than that of pure  $\alpha$ -Fe. It shows that some B atoms enter the  $\alpha$ -Fe lattice to form the  $\alpha$ -Fe(B) solid solution for  $\text{Fe}_{84}\text{Zr}_7\text{B}_9$  alloy. With the increase in Co content, the lattice constant first increases up to 21 at.% Co and then decreases. The increase in lattice constants shows that the increase in Co content inhibits the solid solubility of the B atom in  $\alpha$ -Fe. When the ratio of Co is 21 at.%, the lattice constant is close to that of pure  $\alpha$ -Fe. That is to

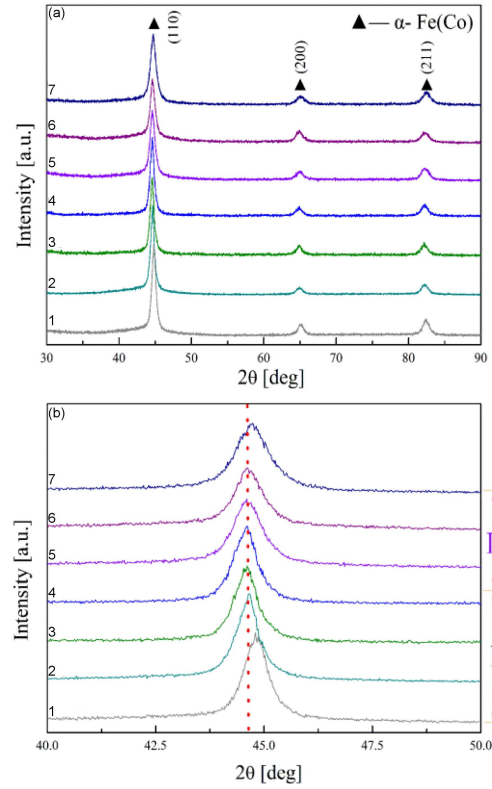


Fig. 3. XRD patterns of  $\text{Fe}_{84-x}\text{Co}_x\text{Zr}_7\text{B}_9$  ( $x = 0, 7, 14, 21, 28, 35, 42$ ) amorphous alloys annealed at the first exothermic peak temperature (a); local area magnification (b); (1)  $\text{Fe}_{84}\text{Zr}_7\text{B}_9$ , (2)  $\text{Fe}_{77}\text{Co}_7\text{Zr}_7\text{B}_9$ , (3)  $\text{Fe}_{70}\text{Co}_{14}\text{Zr}_7\text{B}_9$ , (4)  $\text{Fe}_{63}\text{Co}_{21}\text{Zr}_7\text{B}_9$ , (5)  $\text{Fe}_{56}\text{Co}_{28}\text{Zr}_7\text{B}_9$ , (6)  $\text{Fe}_{49}\text{Co}_{35}\text{Zr}_7\text{B}_9$ , and (7)  $\text{Fe}_{42}\text{Co}_{42}\text{Zr}_7\text{B}_9$ .

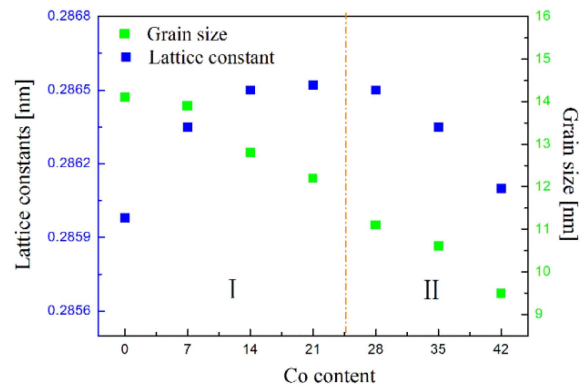


Fig. 4. Grain size and lattice constant of  $\text{Fe}_{84-x}\text{Co}_x\text{Zr}_7\text{B}_9$  ( $x = 0, 7, 14, 21, 28, 35, 42$ ) amorphous alloys annealed at first exothermic peak temperature.

say, few Co/B atoms dissolve in  $\alpha$ -Fe, and Co/B atoms are mainly distributed into the residual amorphous matrix. With the further increase of Co content, the lattice constant decreases and is lower than that of pure  $\alpha$ -Fe, indicating that some Co dissolves in  $\alpha$ -Fe gradually.

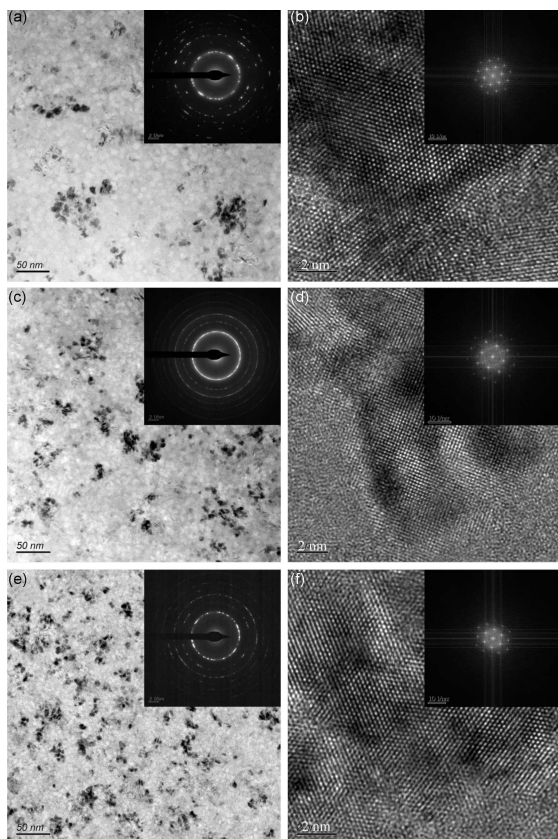


Fig. 5. TEM images, SAED patterns, and HRTEM images of (a, b)  $\text{Fe}_{84}\text{Zr}_7\text{B}_9$ , (c, d)  $\text{Fe}_{63}\text{Co}_{21}\text{Zr}_7\text{B}_9$ , and (e, f)  $\text{Fe}_{42}\text{Co}_{42}\text{Zr}_7\text{B}_9$ .

The transmission electron microscopy (TEM) images, the corresponding selected-area electron diffraction (SAED) patterns, and the high-resolution transmission electron microscope (HRTEM) images of  $\text{Fe}_{84}\text{Zr}_7\text{B}_9$  (a, b),  $\text{Fe}_{63}\text{Co}_{21}\text{Zr}_7\text{B}_9$  (c, d), and  $\text{Fe}_{42}\text{Co}_{42}\text{Zr}_7\text{B}_9$  (e, f) alloys after annealing at their first crystallization peak are shown in Fig. 5. Polycrystalline electron diffraction patterns confirm that only  $\alpha$ -Fe phase precipitates in three kinds of alloys. As seen from the TEM images,  $\alpha$ -Fe nanocrystals are surrounded by the remaining amorphous matrix. It can be seen that the grain size decreases significantly with the increase in Co content. The HRTEM images and corresponding diffraction pattern after fast Fourier transform (FFT) conversion are presented in Fig. 5b, 5d, 5f. They indicate that the grains are all  $\alpha$ -Fe phase grains.

Figure 6 shows the TEM images (a–c) and scanning transmission electron microscopy with energy-dispersive X-ray spectroscopy (STEM-EDS) line-scans (d–f) of  $\text{Fe}_{84}\text{Zr}_7\text{B}_9$ ,  $\text{Fe}_{63}\text{Co}_{21}\text{Zr}_7\text{B}_9$ , and  $\text{Fe}_{42}\text{Co}_{42}\text{Zr}_7\text{B}_9$  amorphous alloys after annealing. For  $\text{Fe}_{84}\text{Zr}_7\text{B}_9$  alloy, Zr is enriched in the remaining amorphous phase. The Zr-depleted region is bcc primary crystals. The primary nanocrystal does not contain Zr and contains lots of Fe. The other part of

Fe is distributed in the remaining amorphous matrix. For  $\text{Fe}_{63}\text{Co}_{21}\text{Zr}_7\text{B}_9$  alloy, Zr is also enriched in the remaining amorphous phase. The nanocrystal does not contain Zr and contains lots of Fe and some Co. The Zr and the other part of Fe and Co are distributed in the remaining amorphous matrix. There is little change in Co concentration between the nanocrystal and the remaining amorphous matrix. For  $\text{Fe}_{42}\text{Co}_{42}\text{Zr}_7\text{B}_9$  alloy, Zr is enriched in the remaining amorphous phase. The nanocrystal does not contain Zr and contains many Fe and Co. The content of Fe in the remaining amorphous matrix is significantly less than that in the nanocrystal. The content of Co in the remaining amorphous matrix is slightly higher than that in the nanocrystal. This is similar to the study of the result by Ping et al. [5]. These authors reported that for  $\text{Fe}_{44}\text{Co}_{44}\text{Zr}_7\text{B}_4\text{Cu}_1$  alloy, Co was preferentially partitioned in the remaining amorphous phase, which was attributed to the large negative heat of mixing between Co and Zr atoms.

The specific saturation magnetization ( $M_s$ ) and coercivity ( $H_c$ ) of the as-quenched  $\text{Fe}_{84-x}\text{Co}_x\text{Zr}_7\text{B}_9$  ( $x = 0, 7, 14, 21, 28, 35, 42$ ) alloys and the annealed alloys are given in Fig. 7. The saturation magnetization  $M_s$  of the as-quenched alloys increases sharply up to 28 at.% Co and then decreases with a further increase in the Co content. The variation in  $M_s$  of the annealed alloys is similar to that of the as-quenched alloys. All the  $M_s$  values of the annealed alloys are greater than those of the as-quenched alloys. It is worth noting that a high Co content does not necessarily ensure a high  $M_s$  value. The  $M_s$  values first increase with increasing Co content and then decrease with a further increase in the Co content. Similar results were obtained for other FeCo-based alloys [15, 22].

The coercivity  $H_c$  of the as-quenched alloys varies negligibly with increasing Co content. The variation in  $H_c$  of the annealed alloys is remarkably different —  $H_c$  decreases rapidly up to 21 at.% Co and changes only negligibly with further increase in the Co content. For the amorphous nanocrystalline two-phase alloy, the intergranular magnetic coupling between adjacent nanocrystals through the residual amorphous phase suppresses the magnetocrystalline anisotropy, affording excellent soft magnetic properties. Suzuki et al. [23] revealed that  $H_c$  is directly proportional to  $D^3$  and  $V_{\text{cry}}$ . In addition to grain size  $D$  and crystallization volume fraction  $V_{\text{cry}}$ , the value of  $H_c$  is also related to the uniformity of grain distribution. For the  $\text{Fe}_{83}\text{Zr}_7\text{B}_9$  alloy,  $D$  and  $V_{\text{cry}}$  are relatively large. Moreover, grain agglomeration is evident, and therefore,  $H_c$  is large. Both  $D$  and  $V_{\text{cry}}$  decrease with increasing Co content, thereby leading to a decrease in  $H_c$ . However, the magneto-crystalline anisotropy constant of  $\alpha$ -Fe(Co) is greater than that of  $\alpha$ -Fe [24]. For  $\text{Fe}_{84-x}\text{Co}_x\text{Zr}_7\text{B}_9$  ( $x = 28, 35, 42$ ) alloys, the decrease in  $H_c$  is small, even if the grain size continues to decrease with increasing

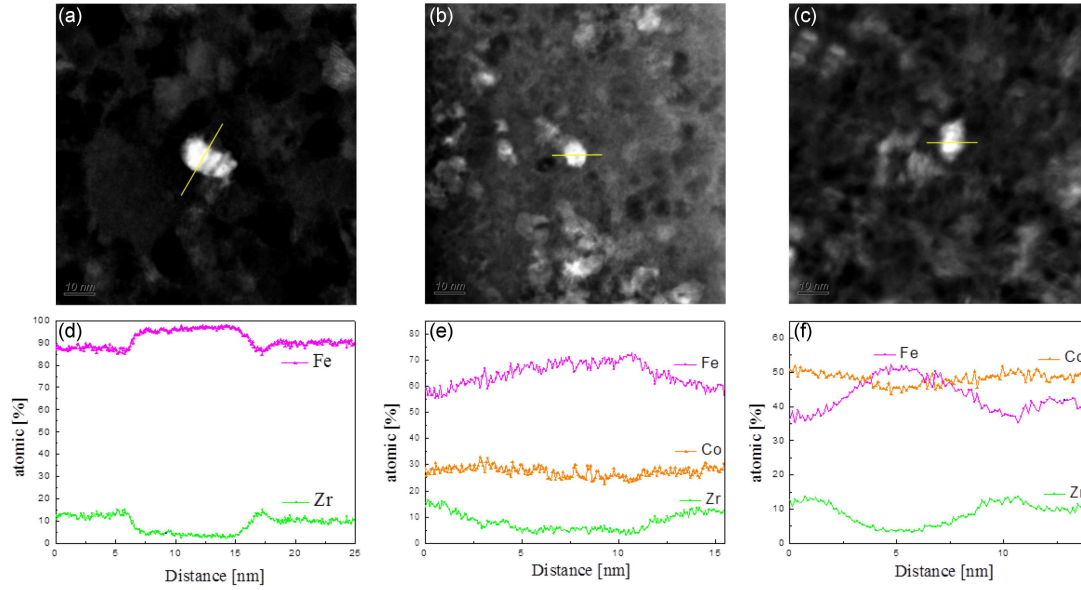


Fig. 6. TEM image (a–c), and STEM-EDS line-scan (d–f) of three kinds of amorphous alloy after annealing — (a, d) Fe<sub>84</sub>Zr<sub>7</sub>B<sub>9</sub>; (b, e) Fe<sub>63</sub>Co<sub>21</sub>Zr<sub>7</sub>B<sub>9</sub>; (c, f) Fe<sub>42</sub>Co<sub>42</sub>Zr<sub>7</sub>B<sub>9</sub>.

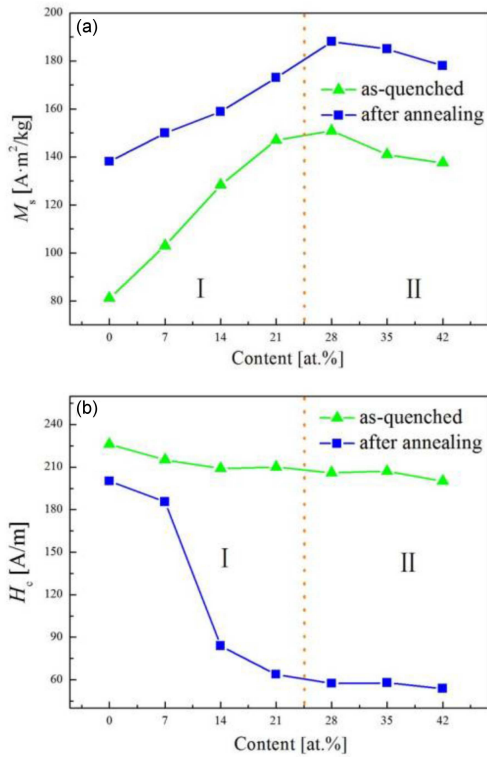


Fig. 7. (a) Specific saturation magnetization ( $M_s$ ) and (b) coercivity ( $H_c$ ) of as-quenched Fe<sub>84-x</sub>Co<sub>x</sub>Zr<sub>7</sub>B<sub>9</sub> ( $x = 0, 7, 14, 21, 28, 35, 42$ ) alloys and the annealed alloys.

Co content. All the  $H_c$  values of the annealed alloys are lower than those of the as-quenched alloys. For Fe<sub>84-x</sub>Co<sub>x</sub>Zr<sub>7</sub>B<sub>9</sub> ( $x = 0, 7, 14, 21$ ) alloys, the higher the Co content, the higher the difference

between the  $H_c$  values of the as-quenched and annealed alloys. For Fe<sub>84-x</sub>Co<sub>x</sub>Zr<sub>7</sub>B<sub>9</sub> ( $x = 28, 35, 42$ ) alloys, the difference between the  $H_c$  values of the as-quenched and annealed alloys changes little.

#### 4. Conclusions

1. Fe<sub>84-x</sub>Co<sub>x</sub>Zr<sub>7</sub>B<sub>9</sub> ( $x = 0, 7, 14, 21, 28, 35, 42$ ) nanocrystalline alloys consisting of bcc nanograins embedded in the residual amorphous matrix were produced by crystallization of amorphous alloys. The crystallization and magnetic properties can be divided into two regions.
2. There are four exothermic peaks for Fe<sub>84-x</sub>Co<sub>x</sub>Zr<sub>7</sub>B<sub>9</sub> ( $x = 0, 7, 14, 21$ ) alloys, and there are three crystallization exothermic peaks for Fe<sub>84-x</sub>Co<sub>x</sub>Zr<sub>7</sub>B<sub>9</sub> ( $x = 28, 35, 42$ ) alloys during the crystallization.
3. The  $\alpha$ -Fe(B) phase precipitates from amorphous matrix for Fe<sub>84</sub>Zr<sub>7</sub>B<sub>9</sub> alloy after annealing. With the increase in Co content, the lattice constant first increases up to 21at.% Co and then decreases. For Fe<sub>84-x</sub>Co<sub>x</sub>Zr<sub>7</sub>B<sub>9</sub> ( $x = 0, 7, 14, 21$ ) alloys, the increase in Co content inhibits the solid solubility of B atom in  $\alpha$ -Fe. For Fe<sub>84-x</sub>Co<sub>x</sub>Zr<sub>7</sub>B<sub>9</sub> ( $x = 28, 35, 42$ ) alloys, Co dissolves in  $\alpha$ -Fe gradually. With the increase in Co content, the crystallization volume fraction and grain size continue to decrease.
4. The grain size decreases significantly with the increase in Co content observed by TEM. For Fe<sub>84</sub>Zr<sub>7</sub>B<sub>9</sub> alloy, Zr is enriched in the remaining amorphous phase. The primary

nanocrystal contains lots of Fe, and the other part of Fe are distributed in the remaining amorphous matrix. For  $\text{Fe}_{63}\text{Co}_{21}\text{Zr}_7\text{B}_9$  alloy, the nanocrystal does not contain Zr and contains lots of Fe and some Co. There is little change in Co concentration between the nanocrystal and the remaining amorphous matrix. For  $\text{Fe}_{42}\text{Co}_{42}\text{Zr}_7\text{B}_9$  alloy, the content of Fe in the remaining amorphous matrix is significantly lower than that in the nanocrystal, and the content of Co in the remaining amorphous matrix is slightly higher than that in the nanocrystal. The content of Fe in the nanocrystal is higher than that of Co in the nanocrystal.

5. The saturation magnetization  $M_s$  of both the as-quenched alloys and the annealed alloys increases sharply up to 28 at.% Co and then decreases with a further increase in the Co content. All the  $M_s$  values of the annealed alloys are greater than those of the as-quenched alloys.
6. The coercivity  $H_c$  of the as-quenched alloys changes little with the increase in Co content.  $H_c$  of the alloys after annealing decreases rapidly up to 21 at.% Co and changes little with the further increase in Co content.  $H_c$  values of the alloys after annealing are all lower than those of the as-quenched alloys. For  $\text{Fe}_{84-x}\text{Co}_x\text{Zr}_7\text{B}_9$  ( $x = 0, 7, 14, 21$ ) alloys, the higher the Co content is, the higher the difference in  $H_c$  between alloys as-quenched and after annealing is. For  $\text{Fe}_{84-x}\text{Co}_x\text{Zr}_7\text{B}_9$  ( $x = 28, 35, 42$ ) alloys, the difference in  $H_c$  between alloys as-quenched and after annealing changes little.

### Acknowledgments

This work was supported by the Natural Science Foundation of Jilin Province (YDZJ202201ZYTS319) and the Sinoma Institute of Materials Research (Guang Zhou) Co., Ltd.

### References

- [1] M. Nabiałek, B. Jeż, K. Bloch, *Metall. Mater. Trans. A* **51**, 4602 (2020).
- [2] S. Lesz, P. Kwapuliński, M. Nabiałek, P. Zackiewicz, L. Hawelek, *J. Therm. Anal. Calorim.* **125**, 1143 (2016).
- [3] B. Kunca, J. Marcin, R. Parsons, P. Švec, P. Švec sr., K. Suzuki, I. Škorvánek, *J. Alloys Compd.* **911**, 165033 (2022).
- [4] M. Nabiałek, S. Walters, P. Vizureanu, M.M.A.B. Abdullah, B. Jeż, *Acta Phys. Pol. A* **138**, 152 (2020).
- [5] D.H. Ping, Y.Q. Wu, K. Hono, M.A. Willard, M.E. McHenry, D.E. Laughlin, *Scr. Mater.* **45**, 781 (2001).
- [6] Y. Gu, Y.H. Zhang, X. Li, J. Wang, B. Wang, K.M. Wang, *Phys. Met. Metallogr.* **121**, 123 (2020).
- [7] M. Ohnuma, D.H. Ping, T. Abe, H. Onodera, K. Hono, Y. Yoshizawa, *J. Appl. Phys.* **93**, 9186 (2003).
- [8] L. Hawelek, M. Polak, P. Włodarczyk, P. Zackiewicz, A. Radon, D. Lukowicz, M. Hreczka, A. Kolano-Burian, *J. Magn. Magn. Mater.* **512**, 166681 (2020).
- [9] C. Parra, C.D. Perea, F.J. Bolivar, *Vacuum* **169**, 108911 (2019).
- [10] L. Hou, M. Li, C. Jiang, X. Fan, Q. Luo, S. Chen, P. Song, W. Li, *J. Alloys Compd.* **853**, 157071 (2021).
- [11] R.K. Roy, A.K. Panda, A. Mitra, *J. Magn. Magn. Mater.* **418**, 236 (2016).
- [12] D. Arvindha Babu, B. Majumdar, R. Sarkar, M. Manivel Raja, D. Akhtar, *J. Mater. Res.* **26**, 2065 (2011).
- [13] M. Nabiałek, *J. Alloys Compd.* **642**, 98 (2015).
- [14] X. Liang, J. Ferenc, T. Kulik, A. Slawska-Waniewska, B. Xu, *J. Magn. Magn. Mater.* **284**, 86 (2004).
- [15] K. Markus, X. Xu, A. Marshal et al., *J. Alloys Compd.* **766**, 686 (2018).
- [16] B. Miao, Q. Luo, C. Chang, T. Liu, Y. Zhang, J. Shen, *J. Magn. Magn. Mater.* **477**, 156 (2019).
- [17] M. Nabiałek, B. Jeż, K. Bloch, P. Pietrusiewicz, J. Gondro, *J. Magn. Magn. Mater.* **477**, 214 (2019).
- [18] F.Y. Shu, B. Yang, S.Y. Dong, H.Y. Zhang, B.S. Xu, F.J. Xu, B. Liu, P. He, J.C. Feng, *Appl. Surf. Sci.* **450**, 538 (2018).
- [19] G. Herzer, *Acta Materialia* **61**, 718 (2013).
- [20] S. He, K. He, B. Shen, H. Zhang, S. Zhang, H. Guo, *J. Appl. Phys.* **86**, 6301 (1999).
- [21] A. Takeuchi, A. Inoue, *Materials Transactions* **46**, 2817 (2005).
- [22] M. Müller, H. Grahl, N. Mattern, U. Kühn, B. Schnell, *J. Magn. Magn. Mater.* **160**, 284 (1996).
- [23] K. Suzuki, G. Herzer, J.M. Cadogan, *J. Magn. Magn. Mater.* **177**, 949 (1998).
- [24] J.J. Ipus, J.S. Blázquez, V. Franco, A. Conde, *J. Alloys Compd.* **496**, 7 (2010).